

Exploring Cation-Deficient Magnetite as a Cathode for Zinc-Ion Aqueous Batteries

Akshatha Venkatesha, Gowra Raghupathy Dillip, Tanmay Mohan Bhagwat, Sayak Mandal, Rekha Kumari, Martin Etter, Gopalakrishnan Sai Gautam, and Aninda J. Bhattacharyya*



Cite This: ACS Sustainable Chem. Eng. 2024, 12, 10411–10422



[Read Online](#)

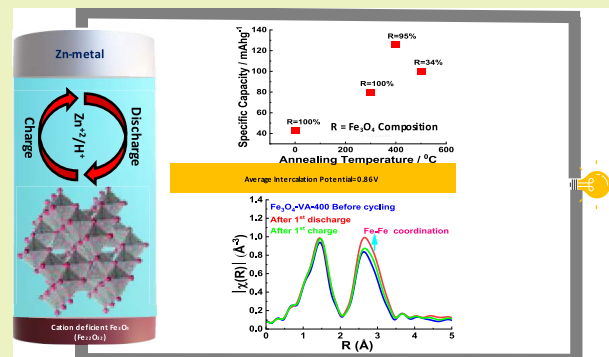
ACCESS ||

Metrics & More

Article Recommendations

SI Supporting Information

ABSTRACT: Zinc-ion aqueous battery (ZIAB) is a promising low-cost alternative, especially for large-scale energy storage applications, e.g., electric grid. The major challenge in ZIABs is the lack of suitable cathode materials, which can intercalate Zn^{2+} ions reversibly over long periods of time. Apart from the availability of suitable cathodes, gaps persist in our fundamental understanding of the mechanisms involved in energy storage in ZIABs. Herein, magnetite (Fe_3O_4) is explored as an alternative cathode for ZIAB. The magnetite cathode is separated from the Zn foil anode by a 1 M aqueous $ZnSO_4$ electrolyte. Annealing of Fe_3O_4 at different temperatures (under moderate vacuum) led to the coexistence of mixed Fe_3O_4 and Fe_2O_3 phases as well as changes in the concentration of cation vacancy. Due to the optimal concentration of both cationic vacancies in Fe_3O_4 and the presence of the Fe_2O_3 phase, the Fe_3O_4 sample annealed at 400 °C exhibits an initial discharge capacity of $\sim 212\text{ mAh g}^{-1}$. Detailed experimental and initial cycle, in addition to Zn ions, results from the coinsertion of H^+ and theoretical calculations show the formation of $Zn_4SO_4(OH)_6 \cdot 4H_2O$, consequence of H^+ coinsertion into the cation-deficient Fe_3O_4 .



bited the best electrochemical performance, with the highest theoretical investigations reveal that the high capacity in the into the cation-deficient Fe_3O_4 . Additionally, both experiment Fe_2O_3 as a byproduct on the cathode surface, which is a direct

KEYWORDS: aqueous zinc-ion batteries, cation-deficient Fe_3O_4 , effect of annealing temperatures on Fe_3O_4 , $\text{Fe}_2\text{O}_3-\text{Fe}_3\text{O}_4$ biphasic mixture, spin-polarized Hubbard U-corrected DFT calculations, $\text{Zn}^{2+}/\text{H}^+$ coininsertion

■ INTRODUCTION

The integration of high-performance rechargeable batteries with conventional/renewable electric grids is an efficient and sustainable strategy for the maximization of electric energy usage. High-energy-density lithium-ion batteries (LIBs), which have been demonstrated in diverse applications, are now being explored as a possible energy storage solution for the electric grid.¹ Considering the high number of deployments spread across diverse economies globally, rechargeable battery chemistry for large-scale deployments must be inexpensive, safe, and environmentally benign. Indeed, lithium-based batteries may not be an effective solution in the long run, and alternative batteries must be rapidly developed.² Notably, aqueous batteries are inexpensive, intrinsically safe, and can potentially displace nonaqueous LIBs for grid-scale storage.^{3–5} Owing to the high theoretical capacity of 819 mAh g⁻¹ and a moderate reduction potential (-0.76 V versus SHE), zinc-ion aqueous batteries (ZIABs) with mildly acidic aqueous electrolytes are a cost-effective and ecofriendly alternative compared to LIBs for grid-scale energy storage.

The challenges associated with ZIABs are diverse and can even outweigh the benefits. ZIABs exhibit nontrivial

physicochemical characteristics of Zn²⁺ and are also plagued by the paucity of Zn²⁺-intercalation materials.⁶ There have been extensive efforts in the development of high-performance cathode materials for ZIABs. Several reports have proposed manganese-based oxides,^{7–23} vanadium-based oxides and sulfides,^{24–36} prussian blue analogs,^{37–43} and organic-based materials^{44–51} as possible cathode materials for ZIABs. However, manganese, vanadium-based oxides, and prussian blue analogs suffer from severe material dissolution into the electrolyte, resulting in structural collapse and capacity decay.⁵² Hence, more efforts are required to unearth feasible oxide-based Zn intercalation electrodes.

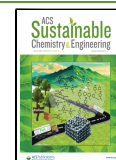
We propose here a magnetite iron oxide (Fe_3O_4) as an inexpensive, scalable, and environment-friendly cathode material for ZIABs.⁵³ Following the initial work by Komaba et

Received: February 29, 2024

Revised: June 21, 2024

Accepted: June 24, 2024

Published: July 1, 2024



al.⁵⁴ Fe_3O_4 has been studied extensively as a conversion electrode in lithium- and sodium-ion batteries.^{55–60} Although Fe_3O_4 has been explored as a cathode in ZIABs,^{61,62} to the best of our knowledge, the fundamental understanding of the influence of structural phase transitions on the energy storage characteristics has not been investigated. Herein, we present detailed experimental and theoretical (using density functional theory (DFT))^{63,64} studies of a ZIAB, where the Fe_3O_4 (pristine and annealed) cathode is separated from the Zn-metal anode by an aqueous ZnSO_4 electrolyte. Structural and spectroscopic analyses reveal interesting structural phase transformations and the creation of cation vacancies in the annealed Fe_3O_4 at selective temperatures. The structural changes significantly affect the underlying electrochemistry and battery performance of the Fe_3O_4 -based ZIABs. Theoretical calculations supported by experimental observations account for the underlying electrochemistry of Fe_3O_4 via the coininsertion of Zn^{2+} and H^+ into the cation-deficient Fe_3O_4 . Our study also confirms the process of H^+ coininsertion into Fe_3O_4 via the $\text{Zn}_4\text{SO}_4(\text{OH})_6 \cdot 4\text{H}_2\text{O}$ complex formation.

EXPERIMENTAL SECTION

Material Procurement. Ferric chloride hexahydrate ($\text{FeCl}_3 \cdot 6\text{H}_2\text{O}$, >99%), poly(ethylene glycol) 400 (PEG 400, >99%), and zinc sulfate heptahydrate ($\text{ZnSO}_4 \cdot 7\text{H}_2\text{O}$, > 99%) are purchased from Merck-Sigma-Aldrich. The sodium hydroxide pellet is brought from Sisco Research Lab Ltd., India. Absolute ethanol (>99.9%) is obtained from Chashu Hongsheng Fine Chemical Co., Ltd., and ethylene glycol (>99%) and cyclopentanone are purchased from Spectrochem Pvt. Ltd., India. The carbon cloth current collector is procured from BAT-SOL Equipment and Technology. Hydrochloric acid (35–38%) is procured from SD Fine-Chem Ltd., India. Zinc foil of 0.25 mm thickness (>99.99%) and carbon black (>99.9%) are obtained from Alfa Aesar. Poly(vinylidene fluoride) (PVDF) is obtained from Kynarflex.

Synthesis of Pristine Fe_3O_4 . The pristine Fe_3O_4 is synthesized using a slightly modified method described by Wang et al.⁶⁵ In brief, 8.1 g of $\text{FeCl}_3 \cdot 6\text{H}_2\text{O}$, 2.58 g of NaOH, and 60 g of PEG 400 are taken and dissolved in 240 mL of ethylene glycol. The mixture is stirred vigorously for 30 min. Further, the mixture is transferred to a 300 mL Teflon-lined autoclave and heated at 200 °C for 10 h. The material is collected by centrifuging at 6000 rpm, which is then washed with ethanol and Millipore water multiple times and dried at 80 °C in a vacuum oven to obtain Fe_3O_4 nanoparticles.

Vacuum Annealing Treatment. The as-synthesized, pristine Fe_3O_4 is divided equally into four portions, out of which three are used for annealing treatment at temperatures 300, 400, and 500 °C. Each portion of Fe_3O_4 for the annealing treatment is taken in an alumina boat and placed in the middle of the quartz tube. The quartz tube is placed in the furnace where one end is connected to a rotary pump and the other is closed by connecting to a tube with a stopper. The quartz tube is evacuated slowly, and the setup is left undisturbed for 30 min until the vacuum level is 400 mmHg (rough vacuum). Subsequently, the sample temperature is ramped up at a heating rate of 10 °C min⁻¹ to 300 °C (or 400/500 °C) and is held at 300 °C (or 400/500 °C) for 5 h. The sample is further analyzed after being cooled to room temperature (RT). The annealed samples are abbreviated as $\text{Fe}_3\text{O}_4\text{-VA-300}$, $\text{Fe}_3\text{O}_4\text{-VA-400}$, and $\text{Fe}_3\text{O}_4\text{-VA-500}$, respectively.

Structural Characterization. The powder X-ray diffraction (PXRD) of all four samples is measured using a PANalytical diffractometer with a Cu-K α radiation of wavelength 0.1542 nm. The XRD pattern refinement is performed using XPert HighScore Plus commercial software (Version: 3.0, PANalytical BV) using the Rietveld method. Fourier-transform infrared (FTIR) is recorded using a Bruker Tensor 27 platinum ATR spectrometer using the Opus software at a spectral resolution of around 1 cm⁻¹. Thermogravimetric

analysis data were collected on a Metler Toledo TGA/SDTA851^e by heating the samples from RT to 900 °C at a heating rate of 10 °C min⁻¹ under a nitrogen atmosphere. Raman spectra are recorded using a HORIBA LabRam HR Evolution Raman Spectrometer equipped with a 532 nm laser. Scanning electron microscopy for morphological analysis is performed using an Ultra55 FE-SEM Karl Zeiss EDS. The morphology of the samples is further examined using transmission electron microscopy (TEM; JEOL JEM-2100F Field Emission Electron Microscope) operating at 200 kV. Gas adsorption analyses are performed using ultrahigh pure nitrogen (99.9995%) on BELSORP-max. Before the measurements, the samples are degassed at 150 °C under a vacuum for 12 h. Elemental analysis for the intercalating ion into active materials is determined with the help of the X-ray photoelectron spectroscopic (XPS) technique using AXIS ULTRA with an Al K α source. The Thermo Avantage software (version: 5.932, Thermo Scientific) is used for data analysis and quantification.

Ex Situ XAS Measurements. All sample XAS spectra (Fe K-edge) are collected in transmission mode at the P65 beamline of the PETRA III synchrotron radiation source (DESY, Hamburg). Multiple scans of Fe K-edge data are calibrated with the reference Fe-foil, properly aligned, and merged using the Athena program⁶⁶ after correctly subtracting the background and normalizing to edge step 1. Obtained EXAFS $\chi(k)$ oscillations remained well-defined with a negligible noise of up to 12.5 Å⁻¹, and Fourier transformations are performed by using a Hanning window in the range of 3–12.5 Å⁻¹. Using the Artemis program,⁶⁶ the R-space data are fitted in the 1–3.5 Å range with a theoretical model⁶⁷ based on the Fe_3O_4 inverse spinel (JCPDS 75–0033) structure. The scattering paths and their contribution to the EXAFS oscillation are calculated with the FEFF6.0 software.⁶⁸ The amplitude reduction factor (S_0^2) is first evaluated by fitting the Fe-foil K-edge data with the Fe-bcc structure (JCPDS 96–110–0109) by fixing the coordination numbers to the known crystallographic values. An S_0^2 value of 0.77, as obtained from this, is fixed in the EXAFS data fittings of the differently treated Fe_3O_4 composites (except $\text{Fe}_3\text{O}_4\text{-VA-500}$). Three scattering paths, i.e., one Fe–O path, a path between two octahedral Fe ions ($\text{Fe}_{\text{Oct}}\text{-}\text{Fe}_{\text{Oct}}$), and between the octahedral and tetrahedral Fe ions ($\text{Fe}_{\text{Oct/Tetra}}\text{-}\text{Fe}_{\text{Tetra/Oct}}$), are used in the theoretical model. As the contribution of the Fe_2O_3 phase is only about 5%, we used the same model for the $\text{Fe}_3\text{O}_4\text{-VA-400}$ phase mixture. However, having a 34:66 mixture of $\text{Fe}_3\text{O}_4/\text{Fe}_2\text{O}_3$ phases in the $\text{Fe}_3\text{O}_4\text{-VA-500}$ phase mixture made it challenging to model the EXAFS data of $\text{Fe}_3\text{O}_4\text{-VA-500}$ properly. For each phase mixture, data of the three different states (before cycling, discharge, and charge) are fitted simultaneously, and to estimate the coordination numbers of the different paths with greater accuracy, we fixed the pseudo/EXAFS Debye–Waller factor to the optimized values in the final fit.

Electrochemical Characterization. The redox behavior of all four samples is studied using the cyclic voltammetry technique with a Biologic SP-300 instrument in the potential range of 0.2–1.8 V versus Zn^{2+}/Zn . The scan rate used here is 0.5 mV s⁻¹. The electrochemical impedance data are measured in the frequency range of 10 mHz to 1 MHz at an amplitude of 5 mV. The quantitative analysis of the impedance data is performed using Zfit software. The galvanostatic charge and discharge cycling are recorded using the Neware battery testing system at a 15 mA g⁻¹ current density. The GITT measurements are carried out in an Arbin instrument. The cell is discharged first for 20 min followed by 20 min of rest. The process is continued until the discharge cutoff voltage is reached. Similar experimental measures are carried out during the first charge process as well. The value of the diffusion coefficient is calculated using the following formula

$$D = \frac{4}{\pi t} \left(\frac{m_b V_m}{M_b S} \right)^2 \left(\frac{\Delta E_s}{\Delta E_t} \right)^2 \quad (1)$$

where D is the diffusion ion coefficient.

Electrochemical Cell Assembly. The electrochemical characterization is performed using CR2032 coin cells (BAT-SOL) using

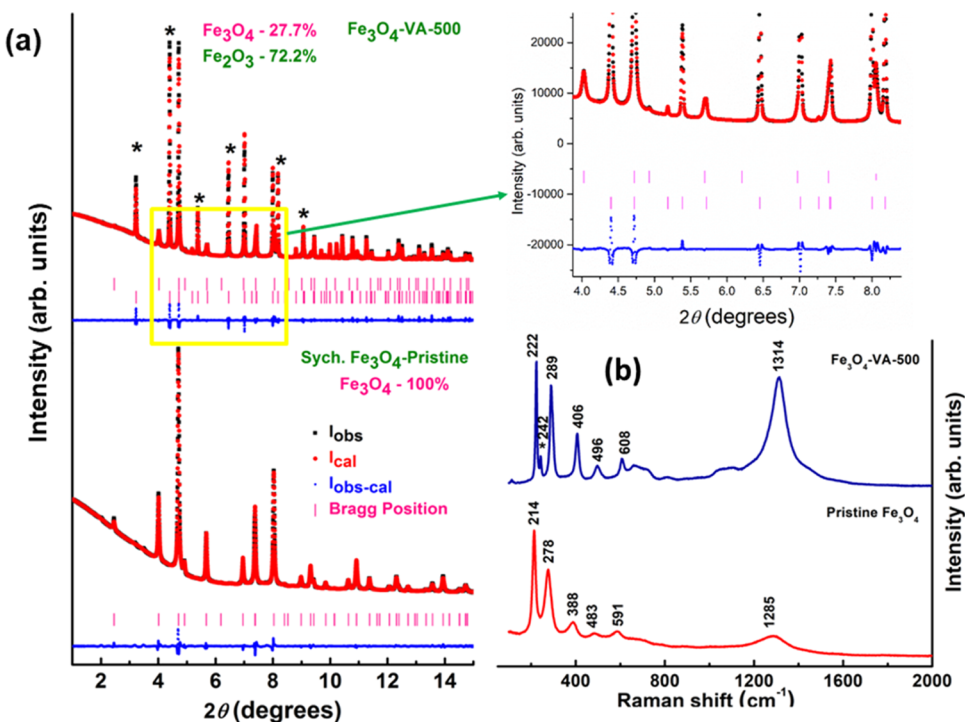


Figure 1. (a) High-resolution synchrotron powder X-ray diffraction (PXRD) of pristine Fe_3O_4 (magnetite) and Fe_3O_4 -VA-500 (mixture of magnetite and hematite). The 2θ values at $2.45^\circ(111)$, $4.01^\circ(220)$, $4.70^\circ(311)$, $4.91^\circ(222)$, $5.68^\circ(400)$, $6.95^\circ(422)$, $7.38^\circ(511)$, and $8.03^\circ(440)$ correspond to the cubic magnetite structure. The additional lines marked by an asterisk in Fe_3O_4 -VA-500 indicate the presence of the hematite (α - Fe_2O_3) phase ($3.22^\circ(012)$, $4.39^\circ(104)$, $5.38^\circ(113)$, $6.44^\circ(024)$, and $8.05^\circ(300)$). (b) Raman spectra of pristine Fe_3O_4 and Fe_3O_4 -VA-500. The Raman bands corresponding to the α - Fe_2O_3 phase are present in the Fe_3O_4 -VA-500 sample in addition to Fe_3O_4 strongly, suggesting the coexistence of Fe_3O_4 and α - Fe_2O_3 in the vacuum-annealed samples at temperatures higher than 300°C in conjunction with PXRD.

pristine Fe_3O_4 , and the three annealed samples as working electrodes, zinc foil as counter and reference electrodes, glass wool as a separator, and 1 M ZnSO_4 dissolved in Millipore water as the electrolyte. The working electrodes are prepared by making a slurry of active materials, conducting carbon black, and poly(vinylidene fluoride) (PVDF) binder in the ratio of 8:1:1. Cyclopentanone solvent is used to prepare the slurry and is drop-cast on a carbon cloth current collector. The mass loading of active material is $\sim 2\text{--}3 \text{ mg cm}^{-2}$. The cells are assembled in ambient conditions without using any glovebox. Before the cell assembly, the electrolytes are purged with a N_2 gas for 40 min to remove the dissolved oxygen in the electrolyte, which might result in parasitic reactions.

DFT Calculations. Spin-polarized Hubbard U -corrected DFT calculations⁶⁹ are performed to identify possible spontaneous reactions during the electrochemical cycling of the $\text{Zn}-\text{Fe}_3\text{O}_4$ in the presence of water using the Vienna Ab-Initio Simulation Package (VASP)^{70,71} and the all-electron, frozen core projector-augmented wave (PAW)⁷² potentials. The rotationally invariant U framework developed by Dudarev et al.⁷³ is used, along with the strongly constrained and appropriately normed (SCAN)⁷⁴ functional, to describe the electronic exchange–correlation interactions. An effective U correction of 3.1 eV is applied on the d orbitals of Fe, as derived in previous work,^{75,76} in all oxides considered, while only SCAN is used for calculating elemental Fe in its body-centered-cubic state. The one-electron wave functions are expanded using a plane-wave basis set with a kinetic energy cutoff of 520 eV, and we kept the convergence parameters for total energies and atomic forces to be 10^{-5} and $10.031 \text{ eV}/\text{\AA}$, respectively. To describe its antiferromagnetic ground state, we use a stricter convergence criterion of 10^{-6} eV for FeO on the total energy.⁷⁷ The relaxation of cell sizes, shapes, and ionic positions is allowed without symmetry restrictions when calculating the total energies of all solids.

In the case of molecular systems, such as H_2 and H_2O , a single molecule of each system is placed in an orthorhombic box ($18 \times 19 \times 20 \text{ \AA}^3$ for both), and we allow for the change in the ionic positions

only. The $\text{Al}\Gamma$ -centered Monkhorst–Pack⁷⁸ mesh with a density of 32 k -points per \AA is used to sample the irreducible Brillouin zone, except in the cases of H_2 and H_2O molecules, where only the Γ -point is sampled. The unrelaxed geometries for all solids are taken from the inorganic crystal structure database (ICSD).⁷⁹ We use a ferromagnetic spin initialization for all Zn- and H-intercalated structures of stoichiometric and cation-deficient Fe_3O_4 . At the same time, we consider the known antiferromagnetic ground-state configurations while calculating FeO , Fe_3O_4 , and Fe_2O_3 .⁷⁵ We use the experimental structural refinement from prior literature^{80,81} to obtain the initial structure of $\text{Zn}_4\text{SO}_4(\text{OH})_6 \cdot 4\text{H}_2\text{O}$. For identifying and relaxing H-positions in calculations, we used the strategy of Gautam et al.,⁸² along with using pymatgen⁸³ for obtaining the initial H-positions.

We introduce two correction schemes to calculate reaction enthalpies in this work: (i) to account for the underestimation of the formation energy of ZnO by SCAN (by -0.29 eV/f.u.),⁷⁶ we reduced the SCAN-calculated total energy of ZnO and (ii) to ensure that SCAN and SCAN + U-calculated total energies can be used for reactions involving Fe, we introduce a correction term to increase the SCAN-calculated total energy of pure Fe (by $+1.1 \text{ eV}$) based on the formation energies of FeO , Fe_2O_3 , and Fe_3O_4 . Any inclusion of experimental (enthalpic and/or entropic) data for calculating reaction enthalpies (along with DFT calculations) is taken from the National Institute of Standards and Technology webbook,⁸⁴ Wagman tables, and/or other experimental literature.⁸⁵ All calculated reaction enthalpies are taken from the corresponding ground-state, relaxed configurations.

RESULTS AND DISCUSSION

Structural Characterization. All samples are thermally stable up to 550°C (Supporting Information: Figure S1), except pristine Fe_3O_4 . The observed changes in the weight loss above 200°C in the annealed samples are significantly less vis-à-vis the pristine sample. This is attributed to the phase

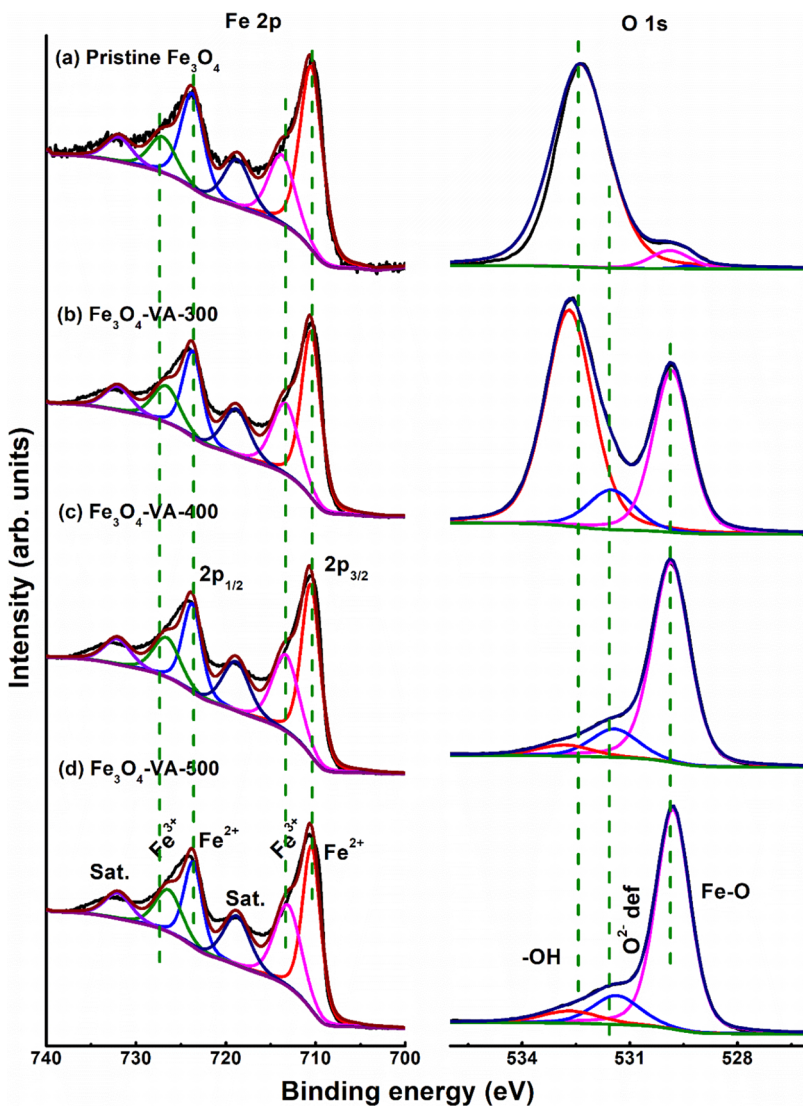


Figure 2. Comparison of XPS core-level spectra of Fe 2p and O 1s of (a) pristine Fe_3O_4 , (b) Fe_3O_4 -VA-300, (c) Fe_3O_4 -VA-400, and (d) Fe_3O_4 -VA-500 samples. The black color indicates the experimental XPS spectra. The color coding of the deconvoluted peaks is as follows: for Fe 2p, red and blue color for Fe^{2+} , magenta and olive green color for Fe^{3+} , and navy blue and violet color for Fe satellite peaks. Purple indicates the baseline, and the wine color is the fit obtained. For the O 1s, the black color indicates the experimental XPS spectra, and magenta, blue, and red colors indicate the deconvoluted O 1s XPS peaks representing metal–oxygen, oxygen defects/vacancies, and surface-adsorbed hydroxyl groups. The green color indicates the baseline, and the navy blue color indicates the fit obtained.

transformation from magnetite to a mixed magnetite–hematite phase in the annealed samples (*vide infra*). All four samples are predominantly nonporous with low BET surface area (Figure S2: type II pattern; ≈ 16 – $53 \text{ m}^2 \text{ g}^{-1}$) and show a cubic/spherical morphology, with sizes ranging from 15 to 45 nm (Figure S3). The transmission electron micrographs for the morphological and particle size analyses of all four samples are shown in Figure S4a–h. It is observed that all of the magnetic nanoparticles are cubic and spherical with relatively different particle sizes (Figure S4a,b,e,f). The particle size distribution graphs are obtained from taking the size of particles at different areas in TEM images and are presented in Figure S4c,d,g,h. The particle size distribution plots revealed that the size of the nanoparticles synthesized varied from 19 to 50 nm in all four samples, and these results obtained are in accordance with the scanning electron microscopic measurements.

Powder X-ray diffraction data are collected using the laboratory as well as at the synchrotron diffractometer (at

P02.1 powder diffraction and total scattering beamline at DESY). The data from both sources and the ensuing analysis are observed to be nearly the same. Owing to higher flux and resolution, for all subsequent studies and analyses, we consider only the high-resolution synchrotron data. The synchrotron powder X-ray diffraction (PXRD), along with the Rietveld refinements, reveals the presence of only a cubic magnetite phase⁶⁵ (Joint Committee on Powder Diffraction Standards—JCPDS 75–0033) in the pristine Fe_3O_4 (Figure 1a) and Fe_3O_4 -VA-300 samples (Figure S5a). The synchrotron PXRD patterns of Fe_3O_4 -VA-400 (Figure S5a) and Fe_3O_4 -VA-500 (Figure 1a), on the other hand, show additional lines marked by an asterisk in Figure 1a (upper diffractogram) and Figure S5a,b, strongly suggesting the concomitant presence of magnetite along with the hematite ($\alpha\text{-Fe}_2\text{O}_3$) phase.⁸⁶ The percentage compositions of magnetite and hematite phases are calculated to be around 94.6 and 5.3% for Fe_3O_4 -VA-400, and 27.7 and 72.2% for Fe_3O_4 -VA-500, respectively. In addition to

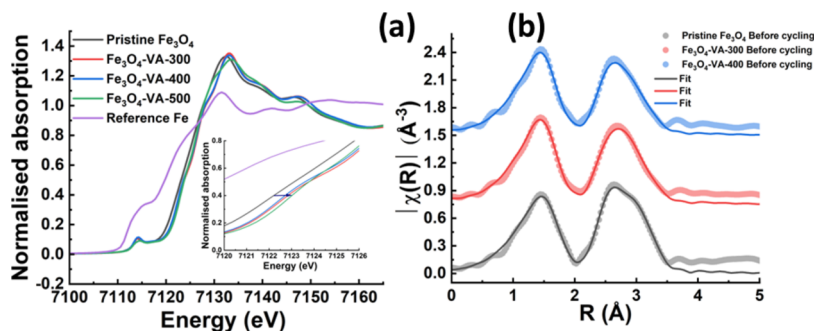


Figure 3. (a) XANES spectra of Fe–K-edge of pristine Fe_3O_4 and all of the vacuum-annealed samples; the inset of (a) zoomed XANES spectra showing the shift in the near-edge region, (b) Fourier transform of the EXAFS oscillation along with the fitting for pristine Fe_3O_4 , Fe_3O_4 -VA-300, and Fe_3O_4 -VA-400.

the presence of mixed phases, from the refinement analysis, cation occupancy (vacancy) in the magnetite phase decreases (increases) with the increase in the annealing temperature. A detailed analysis of the refinement is provided in Table S1: (a) and (b).

The concomitant presence of magnetite and hematite phases in the Fe_3O_4 -VA-400/500 samples as a function of sintering temperature is also supported by Raman scattering measurements (Figures 1b and S6) and Fourier transform infrared (FTIR) spectroscopy (Figure S7). The Fe–O vibrational band around 437 cm^{-1} (Figure S7) shows a slight shift toward a higher wavenumber (by 10 cm^{-1}) in the annealed samples compared to pristine- Fe_3O_4 and becomes more pronounced with an increase in the annealing temperature. This strongly suggests a structural phase transformation due to annealing. The core-level XPS spectra of Fe 2p and O 1s of all four samples are depicted in Figure 2 (c/f Figure S8 for the survey scans.). Despite similar Fe 2p profiles, the estimated atom percentages and the elemental ratio of Fe and O are different (as shown in Table S2). The Fe 2p spectrum of pristine Fe_3O_4 has three doublets related to the Fe^{3+} , Fe^{2+} , and satellite peaks. Among them, the doublets at 710.5 and 723.7 eV correspond to the spin-orbit split of $2p_{3/2}$ and $2p_{1/2}$ for Fe in the 2+ state, while the other two respective peaks at 713.7 and 727.1 eV for Fe in the 3+ state.^{87,88} Similar peaks are also observed in the annealed samples except that the atom percentages in the respective Fe states are different.

The XPS suggests that the samples have mixed valence states of Fe^{3+} and Fe^{2+} (Figure 2). The ratio of $\text{Fe}^{3+}/\text{Fe}^{2+}$ is higher in the annealed samples than in the pristine sample. This suggests that annealing favors the formation of Fe_2O_3 (i.e., Fe^{3+}), which is in line with the observations from the PXRD. O 1s spectra of annealed samples have three peaks: O1 ($\sim 529.8 \text{ eV}$), O2 ($\sim 531.4 \text{ eV}$), and O3 ($\sim 532.7 \text{ eV}$) assigned to the metal–oxygen bonds, oxygen defects/vacancies, and surface hydroxyl groups, respectively.^{88,89} In addition, the following observations are made. (a) The relative atom % of the O3 peak for surface hydroxyl groups decreases from pristine to 500 °C annealed samples. (b) The ratio of O to Fe is increased from pristine to 500 °C annealed samples, confirming an increase in the Fe_2O_3 phase with the increase in annealing temperature. Room-temperature X-ray absorption spectroscopy (XAS) measurements of pristine Fe_3O_4 and all of the annealed samples are carried out to analyze the absorption edges and extended fine structure (i.e., EXAFS) of Fe atoms to obtain insights into the changes in oxidation states, structural evolution, and change in the local coordination environment.

The Fe K-edge X-ray absorption near-edge structure (XANES) spectra of all four samples are shown in Figure 3a.

Figure 3a inset shows a shift in the absorption edge toward the right for the annealed samples compared to the pristine Fe_3O_4 . The extent of the shift is significantly higher with the increase in annealing temperature. This suggests an increase in the oxidation state with an increase in temperature, which supports the formation of Fe_2O_3 , as observed in the PXRD measurements. In addition, the Fourier transform of the EXAFS oscillation (R-space data) of pristine Fe_3O_4 , Fe_3O_4 -VA-300, and Fe_3O_4 -VA-400 samples and their fit with the theoretical model are shown in Figure 3b. The Fe_3O_4 -VA-500 sample is a mixture of Fe_3O_4 and Fe_2O_3 and is not considered for fitting as the analysis and validation of results are nontrivial and may be unphysical. Also, the R-space data and EXAFS $\chi(k)$ oscillations of all four samples are shown in Figure S9a,b. As the EXAFS $\chi(k)$ oscillations remain well-defined with negligible noise for up to 12.5 \AA^{-1} , this region is chosen for the fitting. In the R-space data (phase shift correction not included; Figure 3b), the first feature corresponds to the Fe–O coordination shell, whereas the second feature comprises two Fe–Fe coordination shells.

The EXAFS fitting results for pristine Fe_3O_4 , Fe_3O_4 -VA-300, and Fe_3O_4 -VA-400 are shown in Table S3. Importantly, we observe a decrease in the Fe–O path distance from $1.966(6) \text{ \AA}$ in pristine Fe_3O_4 to $1.933(8) \text{ \AA}$ in Fe_3O_4 -VA-400, which implies an increase in the average oxidation state of Fe, in agreement with the XANES and PXRD data. The pseudo/EXAFS Debye–Waller factor (σ^2) values are higher for the first coordination shell, indicating the presence of multiple Fe–O distances. In addition, a significant change can be observed in the Fe–Fe coordination (both $\text{Fe}_{\text{Oct}}-\text{Fe}_{\text{Oct}}$ and $\text{Fe}_{\text{Oct/Tetra}}-\text{Fe}_{\text{Tetra/Oct}}$). The Fe–Fe coordination number decreases from pristine Fe_3O_4 to Fe_3O_4 -VA-400, strongly suggesting the presence of cation vacancies, which increase with an increase in the annealing temperature. Thus, the findings from XAS are consistent with those of PXRD.

Electrochemical Activity. Cyclic voltammetry (CV at a scan rate of 0.5 mV s^{-1}) confirms the electroactivity of the various Fe_3O_4 samples, as shown in Figure S10. The pristine- Fe_3O_4 , Fe_3O_4 -VA-300, and Fe_3O_4 -VA-400 (in black, blue, and red profiles, respectively; in Figure S10a) electrodes show redox peaks at around 0.8 and 1.16 V versus Zn^{2+}/Zn , attributing to the $\text{Fe}^{2+}/^{3+}$ redox couple (Figure S10b). However, the intensities of these peaks decrease with increasing cycle numbers. In the Fe_3O_4 -VA-500, the redox activity is similar, except that the reduction peaks become

more prominent in the second cycle compared to the first cycle (light green color, Figure S10a,b). In addition, current densities of the redox peaks for all three annealed samples are higher ($75\text{--}125\text{ mA g}^{-1}$) compared to those of the pristine Fe_3O_4 (average value of 60 mA g^{-1}), indicating the enhancement in the electrochemical performance in the annealed sample in comparison to that in the pristine sample.

While the $\text{Fe}_3\text{O}_4\text{-VA-400}$ sample exhibited the highest first cycle specific capacity ($=212\text{ mAhg}^{-1}$) (red color Figure 4),

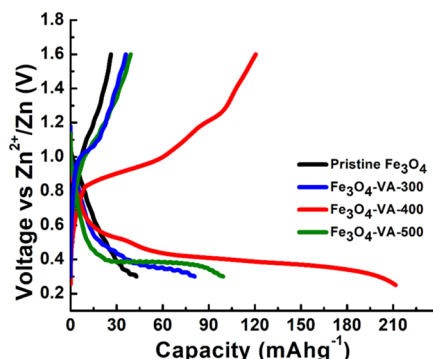


Figure 4. Galvanostatic charge–discharge profiles of pristine Fe_3O_4 , $\text{Fe}_3\text{O}_4\text{-VA-300}$, $\text{Fe}_3\text{O}_4\text{-VA-400}$, and $\text{Fe}_3\text{O}_4\text{-VA-500}$ in a 1 M ZnSO_4 electrolyte in the first cycle at a 15 mA g^{-1} current density.

pristine Fe_3O_4 exhibited the lowest specific capacity of 43 mAh g^{-1} (black color, Figure 4). $\text{Fe}_3\text{O}_4\text{-VA-300}$ (blue color -81 mAh g^{-1}) and $\text{Fe}_3\text{O}_4\text{-VA-500}$ (green color -99 mAh g^{-1}) display capacities intermediate to that of pristine Fe_3O_4 and $\text{Fe}_3\text{O}_4\text{-VA-400}$. The enhanced electrochemical performance in the $\text{Fe}_3\text{O}_4\text{-VA-300/400/500}$ samples can be attributed to the cation vacancies created during annealing. The presence of cation vacancy in the $\text{Fe}_3\text{O}_4\text{-VA-400}$ (best-performing sample) is confirmed by ICP-OES measurements where the concentration of Fe in pristine Fe_3O_4 is found to be 32.21 mg/L and that of $\text{Fe}_3\text{O}_4\text{-VA-400}$ is 12.516 mg/L . Further, the long cyclability and rate capability of the $\text{Zn-Fe}_3\text{O}_4\text{-VA-400}$ cell are carried out (Figure S11a,b). Although the initial capacity is promising, the capacity retention at the end of the 100th cycle (Figure S11a) is inferior, attributed either to the transition-metal dissolution in the acidic aqueous electrolyte or to the irreversible proton intercalation. A systematic approach is required to tackle capacity retention, which is beyond the scope of this work. In addition, the rate capability performed at various current densities such as 12.5 , 25 , 50 , and 100 mA g^{-1} (Figure S11b) depicted that the cell showed reasonably good rate capability when it cycled from a low current density of 12.5 mA g^{-1} to 25 , 50 , and 100 mA g^{-1} current densities. The capacity of the cell increased to a certain extent when the cell was cycled back to lower current densities, such as 50 , 25 , and 12.5 mA g^{-1} .

It is worth mentioning that the electrochemical activity lacks any pseudocapacitive contribution and is predominantly a diffusion-aided process. The value of the constant (exponent), “ b ” in $I_p = av^b$ (where I_p is the peak current, a is a constant, and v is the scan rate; Figures S12 and S13), is found to be nearly 0.5 for both pristine Fe_3O_4 and $\text{Fe}_3\text{O}_4\text{-VA-400}$. Further, the percentage contribution of diffusion and pseudocapacitance (as mentioned in Section S1 and Figures S14 and S15) in pristine Fe_3O_4 and $\text{Fe}_3\text{O}_4\text{-VA-400}$ is calculated to be around 98 and 2% , and 99 and 1% , respectively (Table S4). Thus, the

calculated low values of pseudocapacitance rule out the possibility that cation vacancies assist a pseudocapacitive storage process.

Electrochemical impedance spectroscopy reveals slower charge-transfer resistance (R_{CT}) values for the annealed samples than for the pristine- Fe_3O_4 (Figure S16a,b). The R_{CT} values decrease in general, with successive cycles, with the extent of the decrease being more for the annealed Fe_3O_4 samples than for the pristine sample. The observed decrease in sample R_{CT} with successive cycles could be attributed to the combined effects of the electrochemical activation of Fe_3O_4 and improved electrode wetting. The higher rate of decreased R_{CT} values for the annealed samples is directly attributed to the lower interfacial resistance for the ion transfer across the interface, which arises due to the cation vacancies. This is also supported by GITT measurements, which yielded a slightly lower $\text{Zn}^{2+}/\text{H}^+$ ion diffusion coefficient in the pristine Fe_3O_4 ($\sim 2.00 \times 10^{-9}\text{ cm}^2\text{ s}^{-1}$) compared to that of the $\text{Zn-Fe}_3\text{O}_4\text{-VA-400}$ ($\sim 2.42 \times 10^{-9}\text{ cm}^2\text{ s}^{-1}$), as seen in Figure S16c,d. Improvement in the electrochemical performance of the annealed samples compared with that of the pristine ones can be attributed to the creation of cation vacancies in the annealed samples.

Postelectrochemistry Structural Investigations. Except for the additional line arising at $2\theta \approx 33^\circ$, the PXRD of pristine Fe_3O_4 electrodes after first discharge (shown in red color, Figure S17a) is similar to that of the electrode before cycling (shown in black color, Figure S17a). This line subsides after the first charge (shown in navy blue, Figure S17a). The appearance of this line on the 10th discharge (light green, Figure S17a) and its persistence in the corresponding charge cycle (red wine color, Figure S17a) hint at the possibility of forming an irreversible byproduct. Additionally, a weaker line is observed at $2\theta \approx 9.3^\circ$. These additional peaks may be due to zinc sulfate hydroxide hydrate complex formation. Compared to the pristine Fe_3O_4 electrode, the $\text{Fe}_3\text{O}_4\text{-VA-400}$ shows far more additional peaks after cycling. The $\text{Fe}_3\text{O}_4\text{-VA-400}$ electrode, following the first discharge (shown in wine color, Figure S17b), shows four additional peaks at 2θ values of ≈ 8.6 , 21.4 , 32.9 , and 58.9° . These additional peaks correspond to the reflection planes of zinc sulfate hydroxide hydrate complex viz. $\text{Zn}_4\text{SO}_4(\text{OH})_6\cdot 4\text{H}_2\text{O}$ byproduct (JCPDS 00-044-0673). This byproduct is usually formed when H^+ from the solvent coinerts into the metal oxide cathode along with Zn^{2+} . Simultaneously, the OH^- ions in the solvent can interact with the Zn^{2+} cations, ZnSO_4 salt, and H_2O molecules, forming the sulfate hydroxide complex on the electrode surface. The byproduct formation is consistent with a previous report.⁶¹ Further, the peak intensity slightly reduces upon the first charge (shown in light pink color, Figure S17b), indicating the possibility of reversible conversion of the byproduct. However, the appearance of these lines with successive discharge and the retention after charge strongly suggests an irreversible process (Figure S17b).

The core-level XPS spectra reveal no prominent peaks relating to Zn and S for all samples before cycling (Figures S18–S20 and S5). The peak position and spin–orbit split of Fe $2\text{p}_{1/2}$ and $2\text{p}_{3/2}$ ($13 \pm 0.3\text{ eV}$) for both states ($\text{Fe}^{3+}/\text{Fe}^{2+}$) are similar after the first discharge and charge. While the $\text{Fe}^{3+}/\text{Fe}^{2+}$ reduces for all annealed samples after the first discharge, the $\text{Fe}^{3+}/\text{Fe}^{2+}$ ratio is unchanged for all (including pristine) samples after the first charge (Table S5). This may be due to a partial intercalation–deintercalation of the $\text{Zn}^{2+}/\text{H}^+$ into the

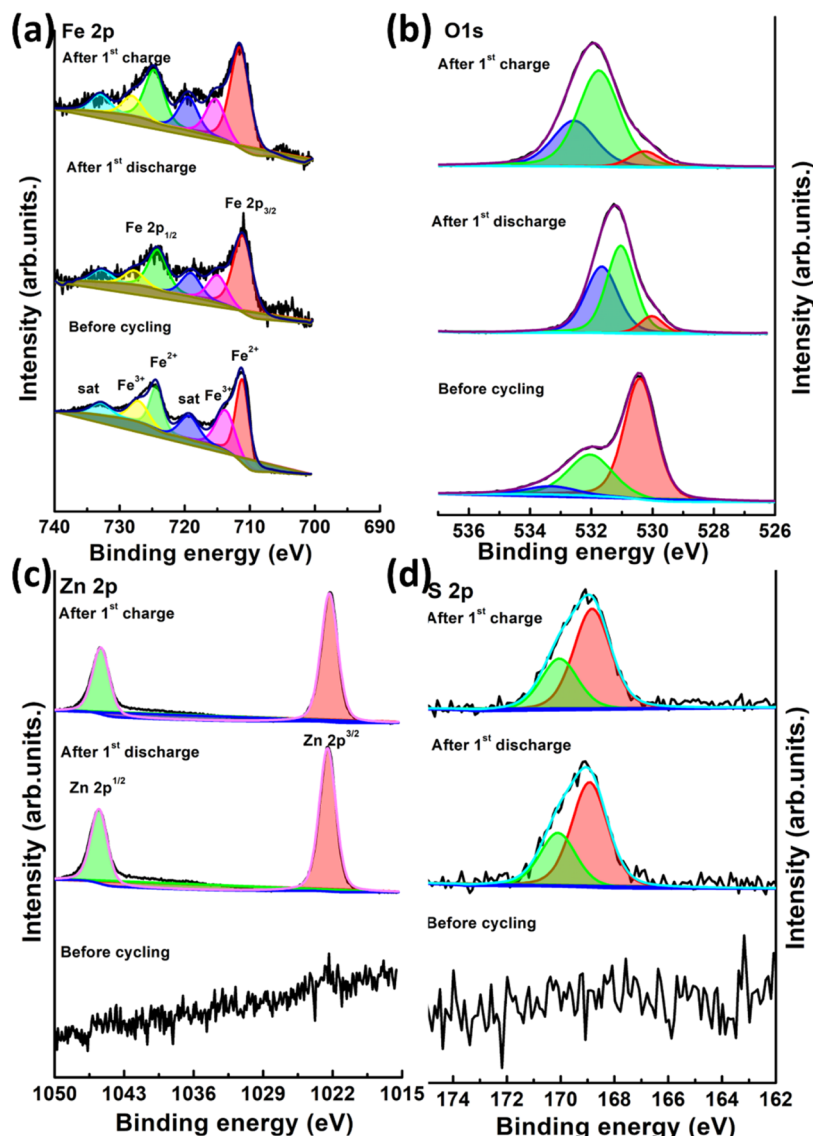


Figure 5. (a–d) XPS spectra of Fe 2p, O 1s, Zn 2p, and S 2p of Fe_3O_4 -VA-400 electrodes before cycling, after the 1st discharge, and the 1st charge, respectively. The black color in all of the XPS spectra is the experimentally obtained spectra. The color coding of deconvoluted peaks is as follows: For Fe 2p, red and green colors for Fe^{2+} , magenta and yellow colors for Fe^{3+} , and blue and cyan colors for Fe satellite peaks. Dark yellow indicates the baseline, and navy blue is the fit obtained. For the O 1s, red, green, and blue colors indicate the deconvoluted O 1s XPS peaks representing metal–oxygen, oxygen defects/vacancies, and surface-adsorbed hydroxyl groups. The cyan color indicates the baseline, and the purple color indicates the fit obtained. For Zn 2p, the red color is for $\text{Zn } 2\text{p}_{3/2}$, the green color is for $\text{Zn } 2\text{p}_{1/2}$, the blue color is the baseline, and the magenta is the fit obtained. For S 2p, red and green colors indicate the deconvoluted peaks, blue indicates the baseline, and cyan color is the fit obtained.

Fe_3O_4 crystal structure. In the case of Zn 2p and S 2p peaks for all electrodes, we observe the standard Zn and S peaks (with the similar spin-orbit split of $\text{Zn } 2\text{p}_{1/2}$ and $2\text{p}_{3/2}$ (23 ± 0.1 eV) and S $2\text{p}_{1/2}$ and $2\text{p}_{3/2}$ (1.2 ± 0.1 eV)) after the first discharge as well as the first charge, confirming the irreversible formation of zinc sulfate hydrate as identified by the ex situ XRD analysis of the cycled electrodes.

Further, the XAS of the pristine- Fe_3O_4 and all of the annealed sample electrodes before and after cycling are measured to determine the structural evolution and change in the local coordination environment of the Fe atoms upon discharge and charge. The XANES spectra of all four samples with cycling show only a slight change in the energy toward a lower value upon discharge. This could be because the change

in oxidation state with discharging may be minimal and is beyond the detection limit of the XAS technique.

In terms of EXAFS (R-space) data, we observe changes with discharging for all four samples, as shown in Figures 6 and S21. To obtain the relevant parameters for the different coordination shells with discharging and charging, the EXAFS (R-space) data of pristine Fe_3O_4 and all of the annealed samples (electrodes before cycling, after first discharge and charge) are fitted as discussed previously (Experimental Section), and the fitting results are tabulated in Tables S6–S9. Although the Fe–O distance does not change significantly with discharging, the Fe–O coordination number increases from 5.95 to 6.43 for pristine Fe_3O_4 and from 5.46 to 6.18 for Fe_3O_4 -VA-400. However, with charging, these values do not return to the original sample values and

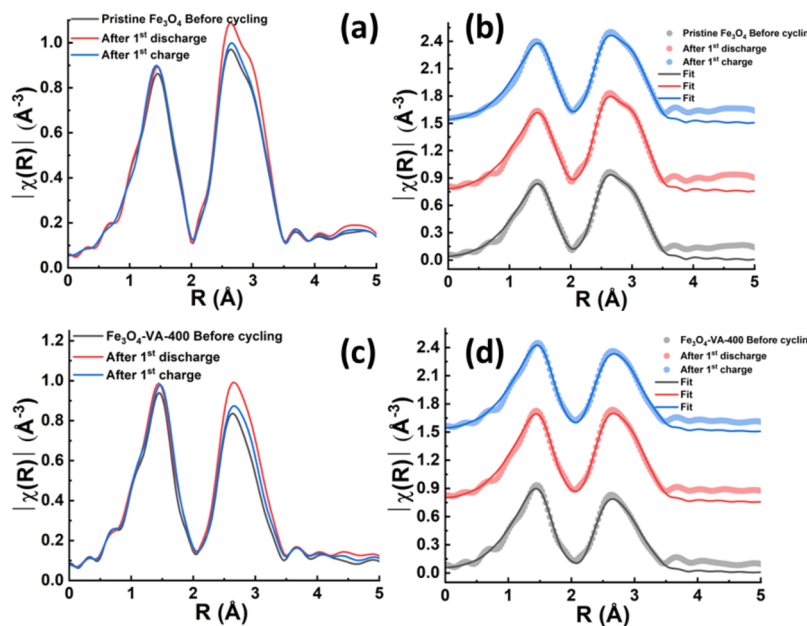


Figure 6. (a, c) Comparison of EXAFS (R-space) data of pristine Fe_3O_4 and Fe_3O_4 -VA-400 before and after cycling, (b, d) Experimental EXAFS (R-space) data and the fitting using theoretical model for pristine Fe_3O_4 and Fe_3O_4 -VA-400.

remain higher (6.17 for pristine Fe_3O_4 and 5.94 for Fe_3O_4 -VA-400). Also, discharging increases the Fe–Fe coordination number for both the second and third shells. These results indicate the occurrence of irreversible transformation of Fe_3O_4 upon discharge, which could be associated with Zn^{2+} and H^+ coininsertion.

DFT Computations. To probe the possible electrochemical reaction(s) that occur in the Zn– Fe_3O_4 system, DFT calculations are utilized to answer three questions: (i) is the electrochemical activity due to stoichiometric or Fe-deficient Fe_3O_4 , (ii) is Zn effecting intercalation or conversion reactions on Fe_3O_4 , and (iii) is H^+ intercalation contributing to the electrochemical response via zinc sulfate hydroxide complex formation. To model a cation-deficient spinel, we consider a $\text{Fe}_{22}\text{O}_{32}$ structure, i.e., Fe_3O_4 with two octahedral Fe-vacancies. We refer conversion reactions as those that lead to a significant change in the composition and structure of the electrode, compared to the case of an intercalation reaction.⁹⁰ For example, the formation of ZnFe_3O_4 from Zn and Fe_3O_4 is an intercalation reaction, while the formation of $\text{ZnO} + \text{Fe}_2\text{O}_3 + \text{FeO}$ is attributed to a conversion reaction.

To understand the contribution of Zn in the electrochemical response, we tabulated possible conversion reactions (Table S10) that Zn can undergo with stoichiometric Fe_3O_4 and a possible intercalation reaction with Fe-deficient $\text{Fe}_{22}\text{O}_{32}$ and calculated their reaction enthalpies using DFT. Table S10 represents the reaction enthalpies as voltages versus the zinc metal. Note that Zn intercalation is stoichiometric, and therefore, Zn intercalation with Fe_3O_4 is not highly likely since this would force Zn and Fe to occupy the empty octahedral sites in the spinel lattice, requiring the movement of several tetrahedral Fe atoms to octahedral sites. Moreover, octahedral coordination is not particularly favorable for Zn.⁹¹ Hence, we expect any Zn intercalation contributions in stoichiometric Fe_3O_4 to be quite marginal, consistent with the experimental PXRD and XPS data.

Importantly, we predict that Zn will react readily with stoichiometric- Fe_3O_4 to form a plethora of conversion

products. Specifically, we find the formation of ZnO and Fe from Zn and Fe_3O_4 to be the most favorable thermodynamically. We also find the formation of ZnFe_2O_4 and ZnO and the $\text{FeO}/\text{Fe}_2\text{O}_3$ formation to be spontaneous thermodynamically. Thus, we expect Zn to spontaneously react with Fe_3O_4 and form a mixture of oxides (ZnO , ZnFe_2O_4 , Fe_2O_3 , FeO , etc.). However, we expect these reaction products to form chiefly at the surface of the Fe_3O_4 spinel since the formation of ZnO can be passivating, preventing further reaction of Zn with the underlying Fe_3O_4 electrode. Therefore, the overall reversible contribution of such spontaneous conversion reactions within our electrochemical system is expected to be low. Such conversion reactions can also explain the significant differences in discharge versus charge capacities.

Also, we observe Zn intercalation to occur spontaneously, resulting in the formation of $\text{Zn}_2\text{Fe}_{22}\text{O}_{32}$, if the cation-deficient spinel is available in the working electrode. Since the formation of cation vacancies is expected to increase with increasing annealing temperatures, the extent of Zn intercalation should also increase with increasing annealing temperatures, resulting in increased electrochemical capacities, which is consistent with our observations (Figure 4). Moreover, the predicted intercalation voltage for Zn in $\text{Fe}_{22}\text{O}_{32}$ is ~ 0.86 V, similar to the average voltage observed in the galvanostatic data (Figure 4). Thus, we expect Zn to contribute reversibly via an intercalation mechanism as the extent of the cation deficiency increases in spinel- Fe_3O_4 .

Apart from Zn intercalation or conversion, a possible side reaction that can contribute to the observed electrochemical capacity, especially when using acidic aqueous electrolytes, is H^+ intercalation. Proton intercalation can detrimentally contribute to capacity fade and accumulation of irreversible capacity during electrochemical cycling.⁸² Proton intercalation may also lead to the formation of the experimentally observed zinc sulfate hydroxide complex. To investigate possible proton intercalation, we consider the formation of two intercalated products, HFe_3O_4 from stoichiometric Fe_3O_4 and $\text{H}_2\text{Fe}_{22}\text{O}_{32}$ from cation-deficient $\text{Fe}_{22}\text{O}_{32}$. The calculated reaction

Table 1. Calculated Enthalpies for Proton and/or Sulfate Hydroxide Complex Reactions with Stoichiometric or Cation-Deficient Fe_3O_4 Spinel

| reaction | calculated enthalpy (eV) |
|--|--------------------------|
| $\text{H}_2(\text{g}) + 2\text{Fe}_3\text{O}_4 \rightarrow 2\text{HFe}_3\text{O}_4$ | 1.86 |
| $\text{H}_2(\text{g}) + \text{Fe}_{22}\text{O}_{32} \rightarrow \text{H}_2\text{Fe}_{22}\text{O}_{32}$ | -1.38 |
| $4\text{Zn} + \text{H}_2\text{SO}_4 + 10\text{H}_2\text{O}(\text{l}) \rightarrow \text{Zn}_4\text{SO}_4(\text{OH})_6 \cdot 4\text{H}_2\text{O} + 4\text{H}_2(\text{g})$ | -4.82 |
| $4\text{Zn} + \text{H}_2\text{SO}_4 + 8\text{Fe}_3\text{O}_4 + 10\text{H}_2\text{O}(\text{l}) \rightarrow \text{Zn}_4\text{SO}_4(\text{OH})_6 \cdot 4\text{H}_2\text{O} + 2\text{HFe}_3\text{O}_4$ | 2.62 |
| $4\text{Zn} + \text{H}_2\text{SO}_4 + 4\text{Fe}_{22}\text{O}_{32} + 10\text{H}_2\text{O}(\text{l})$ | |
| $\rightarrow \text{Zn}_4\text{SO}_4(\text{OH})_6 \cdot 4\text{H}_2\text{O} + 4\text{H}_2\text{Fe}_{22}\text{O}_{32}$ | -10.34 |

enthalpies (at pH = 0) are listed in Table 1, along with relevant reactions involving the sulfate hydroxide complex formation. Note that the final two reactions listed in Table 1 are not pH-dependent and are a summation of either the first and third reactions or the second and third reactions.

Based on our calculated data (Table 1), we do not expect any proton intercalation to occur in the stoichiometric spinel, resulting in the formation of HFe_3O_4 . On the other hand, proton intercalation is predicted to be spontaneous in a cation-deficient spinel, resulting in the formation of $\text{H}_2\text{Fe}_{22}\text{O}_{32}$ (reaction enthalpy remains negative until pH \sim 12). Apart from the acidic electrolyte itself, the formation of $\text{Zn}_4\text{SO}_4(\text{OH})_6 \cdot 4\text{H}_2\text{O}$ by the reaction of Zn and H_2SO_4 can result in the additional formation of free protons, which can in turn contribute to the proton intercalation process. Indeed, we expect the formation of the sulfate hydroxide complex to be spontaneous in the presence of H_2SO_4 , as indicated by the highly negative (~ -4.82 eV) reaction enthalpy. Further, forming the sulfate hydroxide complex can increase the spontaneity of proton intercalation in cation-deficient $\text{Fe}_{22}\text{O}_{32}$, while the complex formation does not increase the driving force sufficiently enough to enable spontaneous proton intercalation in stoichiometric Fe_3O_4 . Thus, we expect proton intercalation to play a significant role as cation vacancies in stoichiometric spinel increase, which is the case with increasing annealing temperatures. Higher proton intercalation will result in higher observed electrochemical capacity during discharge, a lower percentage of capacity being recovered during subsequent charge, and an accelerated capacity fading with the number of cycles, consistent with our electrochemical data.

Finally, we observe from our DFT calculations that reactions involving cation-deficient Fe_3O_4 tend to be more spontaneous, be it Zn intercalation and/or proton intercalation with sulfate hydroxide complex formation, resulting in increased electrochemical capacities observed, at least during the initial cycles. Although cationic vacancies can increase with increasing temperatures, electrochemically inactive Fe_2O_3 phase formation also increases at higher temperatures. Therefore, an optimal annealing temperature, such as 400 °C, can be used to maximize cationic vacancies while minimizing the formation of Fe_2O_3 . Nevertheless, increased electrochemical activity toward Zn intercalation of cation-deficient Fe_3O_4 can also facilitate detrimental proton intercalation. Hence, chemical or electrochemical pathways and/or coating layers can be explored to facilitate Zn intercalation in cation-deficient Fe_3O_4 while suppressing proton intercalation (such as the use of concentrated electrolytes and exploring a hybrid solvent system).^{92,93}

CONCLUSIONS

To conclude, we have demonstrated a simple Zn-ion aqueous battery using a cathode with a well-known crystallographic phase, viz. magnetite Fe_3O_4 . The annealing of magnetite Fe_3O_4 at higher temperatures results in the biphasic mixtures at 400 and 500 °C and cation vacancies in the magnetite phase. The cation vacancies increase with increasing annealing temperature. The electrochemical performance is a function of annealing temperature, with the sample annealed at 400 °C, yielding the highest specific capacity. The improved electrochemical performance is attributed to the combined effects of cation vacancy, which facilitates fast ion transport across the interface and increased ion insertion into the metal oxide. The mechanism of battery operation, analyzed during several ex situ experiments, reveals the coinsertion of Zn^{2+} and H^+ into the metal oxide, which is mediated by the $\text{Zn}_4\text{SO}_4(\text{OH})_6 \cdot 4\text{H}_2\text{O}$ complex formation. The DFT calculations confirmed the battery operational mechanism due to the coinsertion of Zn^{2+} and H^+ in the cation-deficient Fe_3O_4 and the formation of the $\text{Zn}_4\text{SO}_4(\text{OH})_6 \cdot 4\text{H}_2\text{O}$ complex associated with H^+ insertion in the acidic medium. This is in good accordance with the experimental conditions and results. The combined approach of material design and probing of the underlying electrochemical reaction mechanism will open up avenues for the exploration of various earth-abundant materials as hosts for ZIABs.

ASSOCIATED CONTENT

Supporting Information

The Supporting Information is available free of charge at <https://pubs.acs.org/doi/10.1021/acssuschemeng.4c01784>.

Thermogravimetric analysis (TGA), N_2 -adsorption–desorption isotherm, scanning electron micrographs, transmission electron micrographs, synchrotron and lab-scale PXRD, tables containing refinement parameters, RAMAN spectra, FTIR spectra, XPS, EXAFS, table containing EXAFS fitting results, cyclic voltammograms, galvanostatic charge–discharge cycling and rate capability, pseudocapacitance measurements, impedance and GITT, postcycling XRD, XPS, and EXAFS studies, and spin-polarized Hubbard U -corrected DFT calculations (PDF)

AUTHOR INFORMATION

Corresponding Author

Aninda J. Bhattacharyya – Solid State and Structural Chemistry Unit, Indian Institute of Science, Bengaluru 560012, India; Interdisciplinary Centre for Energy Research, Indian Institute of Science, Bengaluru 560012, India;

 orcid.org/0000-0002-0736-0004; Email: anindajb@iisc.ac.in

Authors

Akshatha Venkatesha – *Solid State and Structural Chemistry Unit, Indian Institute of Science, Bengaluru 560012, India*

Gowra Raghupathy Dillip – *Solid State and Structural Chemistry Unit, Indian Institute of Science, Bengaluru 560012, India; Energy Institute, Centre of Rajiv Gandhi Institute of Petroleum Technology, Bengaluru 560064, India;*

 orcid.org/0000-0001-6855-2192

Tanmay Mohan Bhagwat – *Department of Materials Engineering, Indian Institute of Science, Bengaluru 560012, India*

Sayak Mandal – *Solid State and Structural Chemistry Unit, Indian Institute of Science, Bengaluru 560012, India;*

 orcid.org/0009-0002-3932-9404

Rekha Kumari – *Solid State and Structural Chemistry Unit, Indian Institute of Science, Bengaluru 560012, India; Interdisciplinary Centre for Energy Research, Indian Institute of Science, Bengaluru 560012, India*

Martin Etter – *Deutsches Elektronen-Synchrotron (DESY), 22607 Hamburg, Germany*

Gopalakrishnan Sai Gautam – *Department of Materials Engineering, Indian Institute of Science, Bengaluru 560012, India;*  orcid.org/0000-0002-1303-0976

Complete contact information is available at:

<https://pubs.acs.org/10.1021/acssuschemeng.4c01784>

Notes

The authors declare no competing financial interest.

ACKNOWLEDGMENTS

A.V. acknowledges the financial support provided by UGC in the form of a Senior Research Fellowship (SRF), Synchrotron facility at DESY, Germany, for synchrotron XAS and XRD measurements. GRD acknowledges the award of DST-INSPIRE Faculty (DST/INSPIRE/04/2018/000358) and thanks the Department of Science and Technology in New Delhi, India. S.M. acknowledges the Indian Institute of Science, Bengaluru, for student fellowship. R.K. acknowledges financial support provided by FSID/22-23/PC00017. A.J.B. acknowledges the support received under DST/TMD/MECSP/2K17/07. A.J.B. and S.G.G. acknowledge the support received under SERB (IPA/2021/000007). A.J.B. acknowledges J. C. Bose Fellowship, Government of India (JCB/2022/000016). The authors acknowledge the Solid State and Structural Chemistry Unit and Centre for Excellence in Nano Science and Engineering (CeNSE), Indian Institute of Science, Bengaluru, for providing instrumental facilities. The authors also acknowledge the central facility, Inorganic and Physical Chemistry Department (IPC), Indian Institute of Science, for TEM measurements.

REFERENCES

- (1) Choi, D.; Shamim, N.; Crawford, A.; Huang, Q.; Vartanian, C. K.; Viswanathan, V. V.; Paiss, M. D.; Alam, M. J. E.; Reed, D. M.; Sprenkle, V. L. Li-ion battery technology for grid application. *J. Power Sources* **2021**, *511*, No. 230419.
- (2) Whittingham, M. S. Special Editorial Perspective: Beyond Li-Ion Battery Chemistry. *Chem. Rev.* **2020**, *120* (14), 6328–6330.

(3) Fang, G.; Zhou, J.; Pan, A.; Liang, S. Recent Advances in Aqueous Zinc-Ion Batteries. *ACS Energy Lett.* **2018**, *3* (10), 2480–2501.

(4) Kundu, D.; Oberholzer, P.; Glaros, C.; Bouzid, A.; Tervoort, E.; Pasquarello, A.; Niederberger, M. Organic Cathode for Aqueous Zn-Ion Batteries: Taming a Unique Phase Evolution toward Stable Electrochemical Cycling. *Chem. Mater.* **2018**, *30* (11), 3874–3881.

(5) Li, Z.; Ganapathy, S.; Xu, Y.; Zhou, Z.; Sarilar, M.; Wagemaker, M. Mechanistic Insight into the Electrochemical Performance of Zn/VO₂ Batteries with an Aqueous ZnSO₄ Electrolyte. *Adv. Energy Mater.* **2019**, *9* (22), No. 1900237.

(6) Ma, L.; Chen, S.; Long, C.; Li, X.; Zhao, Y.; Liu, Z.; Huang, Z.; Dong, B.; Zapien, J. A.; Zhi, C. Achieving High-Voltage and High-Capacity Aqueous Rechargeable Zinc Ion Battery by Incorporating Two-Species Redox Reaction. *Adv. Energy Mater.* **2019**, *9* (45), No. 1902446.

(7) Zhao, W.; Fee, J.; Khanna, H.; March, S.; Nisly, N.; Rubio, S. J. B.; Cui, C.; Li, Z.; Suib, S. L. A two-electron transfer mechanism of the Zn-doped δ -MnO₂ cathode toward aqueous Zn-ion batteries with ultrahigh capacity. *J. Mater. Chem. A* **2022**, *10* (12), 6762–6771.

(8) Pan, H.; Shao, Y.; Yan, P.; Cheng, Y.; Han, K. S.; Nie, Z.; Wang, C.; Yang, J.; Li, X.; Bhattacharya, P.; Mueller, K. T.; Liu, J. Reversible aqueous zinc/manganese oxide energy storage from conversion reactions. *Nat. Energy* **2016**, *1* (5), No. 16039, DOI: [10.1038/nenergy.2016.39](https://doi.org/10.1038/nenergy.2016.39).

(9) Sun, W.; Wang, F.; Hou, S.; Yang, C.; Fan, X.; Ma, Z.; Gao, T.; Han, F.; Hu, R.; Zhu, M.; Wang, C. Zn/MnO₂ Battery Chemistry With H⁺ and Zn²⁺ Coinsertion. *J. Am. Chem. Soc.* **2017**, *139* (29), 9775–9778.

(10) Wu, B.; Zhang, G.; Yan, M.; Xiong, T.; He, P.; He, L.; Xu, X.; Mai, L. Graphene Scroll-Coated α -MnO₂ Nanowires as High-Performance Cathode Materials for Aqueous Zn-Ion Battery. *Small* **2018**, *14* (13), No. 1703850.

(11) Zhang, N.; Cheng, F.; Liu, J.; Wang, L.; Long, X.; Liu, X.; Li, F.; Chen, J. Rechargeable aqueous zinc-manganese dioxide batteries with high energy and power densities. *Nat. Commun.* **2017**, *8* (1), No. 405.

(12) Li, Y.; Wang, S.; Salvador, J. R.; Wu, J.; Liu, B.; Yang, W.; Yang, J.; Zhang, W.; Liu, J.; Yang, J. Reaction Mechanisms for Long-Life Rechargeable Zn/MnO₂ Batteries. *Chem. Mater.* **2019**, *31* (6), 2036–2047.

(13) Zhao, S.; Han, B.; Zhang, D.; Huang, Q.; Xiao, L.; Chen, L.; Ivey, D. G.; Deng, Y.; Wei, W. Unravelling the reaction chemistry and degradation mechanism in aqueous Zn/MnO₂ rechargeable batteries. *J. Mater. Chem. A* **2018**, *6* (14), 5733–5739.

(14) Wang, D.; Wang, L.; Liang, G.; Li, H.; Liu, Z.; Tang, Z.; Liang, J.; Zhi, C. A Superior δ -MnO₂ Cathode and a Self-Healing Zn- δ -MnO₂ Battery. *ACS Nano* **2019**, *13* (9), 10643–10652.

(15) Alfaruqi, M. H.; Gim, J.; Kim, S.; Song, J.; Jo, J.; Kim, S.; Mathew, V.; Kim, J. Enhanced reversible divalent zinc storage in a structurally stable α -MnO₂ nanorod electrode. *J. Power Sources* **2015**, *288*, 320–327.

(16) Gao, X.; Wu, H.; Li, W.; Tian, Y.; Zhang, Y.; Wu, H.; Yang, L.; Zou, G.; Hou, H.; Ji, X. H⁺ -Insertion Boosted α -MnO₂ for an Aqueous Zn-Ion Battery. *Small* **2020**, *16* (5), No. e1905842.

(17) Alfaruqi, M. H.; Islam, S.; Putro, D. Y.; Mathew, V.; Kim, S.; Jo, J.; Kim, S.; Sun, Y.-K.; Kim, K.; Kim, J. Structural transformation and electrochemical study of layered MnO₂ in rechargeable aqueous zinc-ion battery. *Electrochim. Acta* **2018**, *276*, 1–11.

(18) Wang, J.; Wang, J.-G.; Liu, H.; Wei, C.; Kang, F. Zinc ion stabilized MnO₂ nanospheres for high capacity and long lifespan aqueous zinc-ion batteries. *J. Mater. Chem. A* **2019**, *7* (22), 13727–13735.

(19) Yadav, G. G.; Turney, D.; Huang, J.; Wei, X.; Banerjee, S. Breaking the 2 V Barrier in Aqueous Zinc Chemistry: Creating 2.45 and 2.8 V MnO₂-Zn Aqueous Batteries. *ACS Energy Lett.* **2019**, *4* (9), 2144–2146.

(20) Liu, G.; Huang, H.; Bi, R.; Xiao, X.; Ma, T.; Zhang, L. K⁺ pre-intercalated manganese dioxide with enhanced Zn²⁺ diffusion for high

- rate and durable aqueous zinc-ion batteries. *J. Mater. Chem. A* **2019**, *7* (36), 20806–20812.
- (21) Liu, N.; Wu, X.; Yin, Y.; Chen, A.; Zhao, C.; Guo, Z.; Fan, L.; Zhang, N. Constructing the Efficient Ion Diffusion Pathway by Introducing Oxygen Defects in Mn_2O_3 for High-Performance Aqueous Zinc-Ion Batteries. *ACS Appl. Mater. Interfaces* **2020**, *12* (25), 28199–28205.
- (22) Hao, J.; Mou, J.; Zhang, J.; Dong, L.; Liu, W.; Xu, C.; Kang, F. Electrochemically induced spinel-layered phase transition of Mn_3O_4 in high performance neutral aqueous rechargeable zinc battery. *Electrochim. Acta* **2018**, *259*, 170–178.
- (23) Tan, Q.; Li, X.; Zhang, B.; Chen, X.; Tian, Y.; Wan, H.; Zhang, L.; Miao, L.; Wang, C.; Gan, Y.; Jiang, J.; Wang, Y.; Wang, H. Valence Engineering via In Situ Carbon Reduction on Octahedron Sites Mn_3O_4 for Ultra-Long Cycle Life Aqueous Zn-Ion Battery. *Adv. Energy Mater.* **2020**, *10* (38), No. 2001050.
- (24) Kundu, D.; Adams, B. D.; Duffort, V.; Vajargah, S. H.; Nazar, L. F. A high-capacity and long-life aqueous rechargeable zinc battery using a metal oxide intercalation cathode. *Nat. Energy* **2016**, *1* (10), No. 16119.
- (25) Xia, C.; Guo, J.; Li, P.; Zhang, X.; Alshareef, H. N. Highly Stable Aqueous Zinc-Ion Storage Using a Layered Calcium Vanadium Oxide Bronze Cathode. *Angew. Chem., Int. Ed.* **2018**, *57* (15), 3943–3948.
- (26) He, P.; Zhang, G.; Liao, X.; Yan, M.; Xu, X.; An, Q.; Liu, J.; Mai, L. Sodium Ion Stabilized Vanadium Oxide Nanowire Cathode for High-Performance Zinc-Ion Batteries. *Adv. Energy Mater.* **2018**, *8* (10), No. 1702463.
- (27) Ming, F.; Liang, H.; Lei, Y.; Kandambeth, S.; Eddouadi, M.; Alshareef, H. N. Layered $MgxV_2O_5 \cdot nH_2O$ as Cathode Material for High-Performance Aqueous Zinc Ion Batteries. *ACS Energy Lett.* **2018**, *3* (10), 2602–2609.
- (28) Soundharajan, V.; Sambandam, B.; Kim, S.; Alfaruqi, M. H.; Putro, D. Y.; Jo, J.; Kim, S.; Mathew, V.; Sun, Y. K.; Kim, J. $Na_2V_6O_{16} \cdot 3H_2O$ Barnesite Nanorod: An Open Door to Display a Stable and High Energy for Aqueous Rechargeable Zn-Ion Batteries as Cathodes. *Nano Lett.* **2018**, *18* (4), 2402–2410.
- (29) Zhang, N.; Jia, M.; Dong, Y.; Wang, Y.; Xu, J.; Liu, Y.; Jiao, L.; Cheng, F. Hydrated Layered Vanadium Oxide as a Highly Reversible Cathode for Rechargeable Aqueous Zinc Batteries. *Adv. Funct. Mater.* **2019**, *29* (10), No. 1807331.
- (30) Dai, X.; Wan, F.; Zhang, L.; Cao, H.; Niu, Z. Freestanding graphene/VO₂ composite films for highly stable aqueous Zn-ion batteries with superior rate performance. *Energy Storage Mater.* **2019**, *17*, 143–150.
- (31) Sambandam, B.; Soundharajan, V.; Kim, S.; Alfaruqi, M. H.; Jo, J.; Kim, S.; Mathew, V.; Sun, Y.-k.; Kim, J. Aqueous rechargeable Zn-ion batteries: an imperishable and high-energy $Zn_2V_2O_7$ nanowire cathode through intercalation regulation. *J. Mater. Chem. A* **2018**, *6* (9), 3850–3856.
- (32) Li, Z.; Ren, Y.; Mo, L.; Liu, C.; Hsu, K.; Ding, Y.; Zhang, X.; Li, X.; Hu, L.; Ji, D.; Cao, G. Impacts of Oxygen Vacancies on Zinc Ion Intercalation in VO₂. *ACS Nano* **2020**, *14* (5), 5581–5589.
- (33) Shin, J.; Choi, D. S.; Lee, H. J.; Jung, Y.; Choi, J. W. Hydrated Intercalation for High-Performance Aqueous Zinc Ion Batteries. *Adv. Energy Mater.* **2019**, *9* (14), No. 1900083.
- (34) Gautam, G. S.; Canepa, P.; Malik, R.; Liu, M.; Persson, K.; Ceder, G. First-principles evaluation of multi-valent cation insertion into orthorhombic V₂O₅. *Chem. Commun.* **2015**, *51* (71), 13619–13622.
- (35) Wang, T.; Li, S.; Weng, X.; Gao, L.; Yan, Y.; Zhang, N.; Qu, X.; Jiao, L.; Liu, Y. Ultrafast 3D Hybrid-Ion Transport in Porous V₂O₅ Cathodes for Superior-Rate Rechargeable Aqueous Zinc Batteries. *Adv. Energy Mater.* **2023**, *13* (18), No. 2204358, DOI: [10.1002/aenm.202204358](https://doi.org/10.1002/aenm.202204358).
- (36) Tan, Y.; Li, S.; Zhao, X.; Wang, Y.; Shen, Q.; Qu, X.; Liu, Y.; Jiao, L. Unexpected Role of the Interlayer “Dead Zn²⁺” in Strengthening the Nanostructures of VS₂ Cathodes for High-
- Performance Aqueous Zn-Ion Storage. *Adv. Energy Mater.* **2022**, *12* (19), No. 2104001, DOI: [10.1002/aenm.202104001](https://doi.org/10.1002/aenm.202104001).
- (37) Liu, Z.; Pulletikurthi, G.; Endres, F. A Prussian Blue/Zinc Secondary Battery with a Bio-Ionic Liquid–Water Mixture as Electrolyte. *ACS Appl. Mater. Interfaces* **2016**, *8* (19), 12158–12164.
- (38) Jia, Z.; Wang, B.; Wang, Y. Copper hexacyanoferrate with a well-defined open framework as a positive electrode for aqueous zinc ion batteries. *Mater. Chem. Phys.* **2015**, *149*–150, 601–606.
- (39) Chae, M. S.; Heo, J. W.; Kwak, H. H.; Lee, H.; Hong, S.-T. Organic electrolyte-based rechargeable zinc-ion batteries using potassium nickel hexacyanoferrate as a cathode material. *J. Power Sources* **2017**, *337*, 204–211.
- (40) Huang, M.; Meng, J.; Huang, Z.; Wang, X.; Mai, L. Ultrafast cation insertion-selected zinc hexacyanoferrate for 1.9 V K–Zn hybrid aqueous batteries. *J. Mater. Chem. A* **2020**, *8* (14), 6631–6637.
- (41) Cao, T.; Zhang, F.; Chen, M.; Shao, T.; Li, Z.; Xu, Q.; Cheng, D.; Liu, H.; Xia, Y. Cubic Manganese Potassium Hexacyanoferrate Regulated by Controlling of the Water and Defects as a High-Capacity and Stable Cathode Material for Rechargeable Aqueous Zinc-Ion Batteries. *ACS Appl. Mater. Interfaces* **2021**, *13* (23), 26924–26935.
- (42) Kasiri, G.; Glenneberg, J.; Hashemi, A. B.; Kun, R.; La Mantia, F. Mixed copper-zinc hexacyanoferrates as cathode materials for aqueous zinc-ion batteries. *Energy Storage Mater.* **2019**, *19*, 360–369.
- (43) Wang, L. P.; Wang, P. F.; Wang, T. S.; Yin, Y. X.; Guo, Y. G.; Wang, C. R. Prussian blue nanocubes as cathode materials for aqueous Na-Zn hybrid batteries. *J. Power Sources* **2017**, *355*, 18–22.
- (44) Zhang, S.; Zhao, W.; Li, H.; Xu, Q. Cross-Conjugated Polycatechol Organic Cathode for Aqueous Zinc-Ion Storage. *ChemSusChem* **2020**, *13* (1), 188–195.
- (45) Sun, T.; Li, Z. J.; Zhi, Y. F.; Huang, Y. J.; Fan, H. J.; Zhang, Q. Poly(2,5-Dihydroxy-1,4-Benzoquinonyl Sulfide) As an Efficient Cathode for High-Performance Aqueous Zinc–Organic Batteries. *Adv. Funct. Mater.* **2021**, *31* (16), No. 2010049.
- (46) Wang, Q.; Liu, Y.; Chen, P. Phenazine-based organic cathode for aqueous zinc secondary batteries. *J. Power Sources* **2020**, *468*, No. 228401.
- (47) Zhao, Y.; Wang, Y.; Zhao, Z.; Zhao, J.; Xin, T.; Wang, N.; Liu, J. Achieving high capacity and long life of aqueous rechargeable zinc battery by using nanoporous-carbon-supported poly(1,5-naphthalenediamine) nanorods as cathode. *Energy Storage Mater.* **2020**, *28*, 64–72.
- (48) Wang, N.; Dong, X.; Wang, B.; Guo, Z.; Wang, Z.; Wang, R.; Qiu, X.; Wang, Y. Zinc–Organic Battery with a Wide Operation-Temperature Window from –70 to 150 °C. *Angew. Chem., Int. Ed.* **2020**, *59* (34), 14577–14583.
- (49) Guo, Z.; Ma, Y.; Dong, X.; Huang, J.; Wang, Y.; Xia, Y. An Environmentally Friendly and Flexible Aqueous Zinc Battery Using an Organic Cathode. *Angew. Chem., Int. Ed.* **2018**, *57* (36), 11737–11741.
- (50) Nam, K. W.; Park, S. S.; dos Reis, R.; Dravid, V. P.; Kim, H.; Mirkin, C. A.; Stoddart, J. F. Conductive 2D metal-organic framework for high-performance cathodes in aqueous rechargeable zinc batteries. *Nat. Commun.* **2019**, *10* (1), No. 4948.
- (51) Yeon, J. S.; Kim, W. I.; Kim, H. J.; Jang, G.; Park, J. M.; Park, J. H.; Li, Y.; Park, H. S. Accordion-like polyoxometalate hybrid architectures for capacity-dense and flexible Zn-Ion battery cathodes. *Energy Storage Mater.* **2023**, *63*, No. 102944.
- (52) Kumankuma-Sarpong, J.; Tang, S.; Guo, W.; Fu, Y. Naphthoquinone-Based Composite Cathodes for Aqueous Rechargeable Zinc-Ion Batteries. *ACS Appl. Mater. Interfaces* **2021**, *13* (3), 4084–4092.
- (53) Zhang, W. M.; Wu, X. L.; Hu, J. S.; Guo, Y. G.; Wan, L. J. Carbon Coated Fe₃O₄ Nanospindles as a Superior Anode Material for Lithium-Ion Batteries. *Adv. Funct. Mater.* **2008**, *18* (24), 3941–3946.
- (54) Komaba, S.; Mikumo, T.; Ogata, A. Electrochemical activity of nanocrystalline Fe₃O₄ in aprotic Li and Na salt electrolytes. *Electrochim. Commun.* **2008**, *10* (9), 1276–1279.

- (55) Kumar, P. R.; Jung, Y. H.; Bharathi, K. K.; Lim, C. H.; Kim, D. K. High capacity and low cost spinel Fe_3O_4 for the Na-ion battery negative electrode materials. *Electrochim. Acta* **2014**, *146*, 503–510.
- (56) He, C.; Wu, S.; Zhao, N.; Shi, C.; Liu, E.; Li, J. Carbon-Encapsulated Fe_3O_4 Nanoparticles as a High-Rate Lithium Ion Battery Anode Material. *ACS Nano* **2013**, *7* (5), 4459–4469.
- (57) Zhao, Y.; Wang, F.; Wang, C.; Wang, S.; Wang, C.; Zhao, Z.; Duan, L.; Liu, Y.; Wu, Y.; Li, W.; Zhao, D. Encapsulating highly crystallized mesoporous Fe_3O_4 in hollow N-doped carbon nanospheres for high-capacity long-life sodium-ion batteries. *Nano Energy* **2019**, *56*, 426–433.
- (58) Zhao, Q.; Liu, J.; Wang, Y.; Tian, W.; Liu, J.; Zang, J.; Ning, H.; Yang, C.; Wu, M. Novel in-situ redox synthesis of $\text{Fe}_3\text{O}_4/\text{rGO}$ composites with superior electrochemical performance for lithium-ion batteries. *Electrochim. Acta* **2018**, *262*, 233–240.
- (59) Liu, H.; Jia, M.; Zhu, Q.; Cao, B.; Chen, R.; Wang, Y.; Wu, F.; Xu, B. 3D-0D Graphene- Fe_3O_4 Quantum Dot Hybrids as High-Performance Anode Materials for Sodium-Ion Batteries. *ACS Appl. Mater. Interfaces* **2016**, *8* (40), 26878–26885.
- (60) Zhong, G.; Qu, K.; Ren, C.; Su, Y.; Fu, B.; Zi, M.; Dai, L.; Xiao, Q.; Xu, J.; Zhong, X.; An, F.; Ye, M.; Ke, S.; Xie, S.; Wang, J.; Gao, P.; Li, J. Epitaxial array of Fe_3O_4 nanodots for high rate high capacity conversion type lithium ion batteries electrode with long cycling life. *Nano Energy* **2020**, *74*, No. 104876.
- (61) Wang, Z.; Wang, Y.; Wang, G.; Wu, W.; Zhu, J. Earth-abundant magnetite with carbon coatings as reversible cathodes for stretchable zinc-ion batteries. *J. Energy Chem.* **2021**, *62*, 552–562.
- (62) Liu, W.; Hao, J.; Xu, C.; Mou, J.; Dong, L.; Jiang, F.; Kang, Z.; Wu, J.; Jiang, B.; Kang, F. Investigation of zinc ion storage of transition metal oxides, sulfides, and borides in zinc ion battery systems. *Chem. Commun.* **2017**, *53* (51), 6872–6874.
- (63) Hohenberg, P.; Kohn, W. Inhomogeneous Electron Gas. *Phys. Rev.* **1964**, *136* (3B), No. B864, DOI: 10.1103/PhysRev.136.B864.
- (64) Kohn, W.; Sham, L. J. Self-Consistent Equations Including Exchange and Correlation Effects. *Phys. Rev.* **1965**, *140* (4A), No. A1133, DOI: 10.1103/PhysRev.140.A1133.
- (65) Wang, Y.; Li, Y.; Qiu, Z.; Wu, X.; Zhou, P.; Zhou, T.; Zhao, J.; Miao, Z.; Zhou, J.; Zhuo, S. $\text{Fe}_3\text{O}_4@\text{Ti}_3\text{C}_2$ MXene hybrids with ultrahigh volumetric capacity as an anode material for lithium-ion batteries. *J. Mater. Chem. A* **2018**, *6* (24), 11189–11197.
- (66) Ravel, B.; Newville, M. ATHENA, ARTEMIS, HEPHAESTUS: data analysis for X-ray absorption spectroscopy using IFEFFIT. *J. Synchrotron Radiat.* **2005**, *12* (4), 537–541.
- (67) Gao, L.; Tang, C.; Liu, J.; He, L.; Wang, H.; Ke, Z.; Li, W.; Jiang, C.; He, D.; Cheng, L.; Xiao, X. Oxygen Vacancy-induced Electron Density Tuning of Fe_3O_4 for Enhanced Oxygen Evolution Catalysis. *Energy Environ. Mater.* **2021**, *4* (3), 392–398.
- (68) Zabinsky, S. I.; Rehr, J. J.; Ankudinov, A.; Albers, R. C.; Eller, M. J. Multiple-scattering calculations of x-ray-absorption spectra. *Phys. Rev. B* **1995**, *52* (4), No. 2995, DOI: 10.1103/PhysRevB.52.2995.
- (69) Anisimov, V. I.; Zaanen, J.; Andersen, O. K. Band theory and Mott insulators: Hubbard U instead of Stoner I. *Phys. Rev. B* **1991**, *44* (3), No. 943, DOI: 10.1103/PhysRevB.44.943.
- (70) Kresse, G.; Hafner, J. Ab initio molecular dynamics for liquid metals. *Phys. Rev. B* **1993**, *47* (1), No. 558, DOI: 10.1103/PhysRevB.47.558.
- (71) Kresse, G.; Furthmüller, J. Efficient iterative schemes for ab initio total-energy calculations using a plane-wave basis set. *Phys. Rev. B* **1996**, *54* (16), No. 11169, DOI: 10.1103/PhysRevB.54.11169.
- (72) Kresse, G.; Joubert, D. From ultrasoft pseudopotentials to the projector augmented-wave method. *Phys. Rev. B* **1999**, *59* (3), No. 1758, DOI: 10.1103/PhysRevB.59.1758.
- (73) Dudarev, S. L.; Botton, G. A.; Savrasov, S. Y.; Humphreys, C. J.; Sutton, A. P. Electron-energy-loss spectra and the structural stability of nickel oxide: An LSDA+U study. *Phys. Rev. B* **1998**, *57* (3), No. 1505, DOI: 10.1103/PhysRevB.57.1505.
- (74) Sun, J.; Ruzsinszky, A.; Perdew, J. P. Strongly Constrained and Appropriately Normed Semilocal Density Functional. *Phys. Rev. Lett.* **2015**, *115* (3), No. 036402.
- (75) Gautam, G. S.; Carter, E. A. Evaluating transition metal oxides within DFT-SCAN and SCAN + U frameworks for solar thermochemical applications. *Phys. Rev. Mater.* **2018**, *2* (9), No. 095401.
- (76) Long, O. Y.; Gautam, G. S.; Carter, E. A. Evaluating optimal U for 3d transition-metal oxides within the SCAN + U framework. *Phys. Rev. Mater.* **2020**, *4* (4), No. 045401.
- (77) Roth, W. L. Magnetic Structures of MnO , FeO , CoO , and NiO . *Phys. Rev.* **1958**, *110* (6), No. 1333, DOI: 10.1103/PhysRev.110.1333.
- (78) Monkhorst, H. J.; Pack, J. D. Special points for Brillouin-zone integrations. *Phys. Rev. B* **1976**, *13* (12), No. 5188, DOI: 10.1103/PhysRevB.13.5188.
- (79) Hellenbrandt, M. The Inorganic Crystal Structure Database (ICSD)-Present and Future. *Crystallogr. Rev.* **2004**, *10* (1), 17–22.
- (80) Groat, L. A. The crystal structure of namuwite, a mineral with Zn in tetrahedral and octahedral coordination, and its relationship to the synthetic basic zinc sulfates. *Am. Mineral.* **1996**, *81* (1–2), 238–243.
- (81) Bear, I. J.; Grey, I. E.; Newnham, I. E.; Rogers, L. J. The $\text{ZnSO}_4 \cdot 3\text{Zn}(\text{OH})_2 \cdot \text{H}_2\text{O}$ system. I. Phase formation. *Aust. J. Chem.* **1987**, *40* (3), 539–556.
- (82) Gautam, G. S.; Canepa, P.; Richards, W. D.; Malik, R.; Ceder, G. Role of Structural H_2O in Intercalation Electrodes: The Case of Mg in Nanocrystalline Xerogel- V_2O_5 . *Nano Lett.* **2016**, *16* (4), 2426–2431.
- (83) Ong, S. P.; Richards, W. D.; Jain, A.; Hautier, G.; Kocher, M.; Cholia, S.; Gunter, D.; Chevrier, V. L.; Persson, K. A.; Ceder, G. Python Materials Genomics (pymatgen): A robust, open-source python library for materials analysis. *Comput. Mater. Sci.* **2013**, *68*, 314–319.
- (84) NIST Chemistry WebBook, SRD 69 2023 <https://webbook.nist.gov/chemistry/>.
- (85) Majzlan, J.; Navrotsky, A.; Stevens, R.; Donaldson, M.; Woodfield, B. F.; Boero-Goates, J. Thermodynamics of monoclinic $\text{Fe}_2(\text{SO}_4)_3$. *J. Chem. Thermodyn.* **2005**, *37* (8), 802–809.
- (86) Han, R.; Li, W.; Pan, W.; Zhu, M.; Zhou, D.; Li, F.-s. 1D Magnetic Materials of Fe_3O_4 and Fe with High Performance of Microwave Absorption Fabricated by Electrospinning Method. *Sci. Rep.* **2014**, *4* (1), No. 7493.
- (87) Hiura, S.; Ikeuchi, A.; Shirini, S.; Subagyo, A.; Sueoka, K. Effect of adsorbed H atoms on the Fe electronic states of Fe_3O_4 (001) film surfaces. *Phys. Rev. B* **2015**, *91* (20), No. 205411.
- (88) Hu, X.; Ma, M.; Zeng, M.; Sun, Y.; Chen, L.; Xue, Y.; Zhang, T.; Ai, X.; Mendes, R. G.; Rümmeli, M. H.; Fu, L. Supercritical Carbon Dioxide Anchored Fe_3O_4 Nanoparticles on Graphene Foam and Lithium Battery Performance. *ACS Appl. Mater. Interfaces* **2014**, *6* (24), 22527–22533.
- (89) Fujii, T.; de Groot, F. M. F.; Sawatzky, G. A.; Voigt, F. C.; Hibma, T.; Okada, K. In situ XPS analysis of various iron oxide films grown by NO_2 -assisted molecular-beam epitaxy. *Phys. Rev. B* **1999**, *59* (4), 3195–3202.
- (90) Hannah, D. C.; Gautam, G. S.; Canepa, P.; Ceder, G. On the Balance of Intercalation and Conversion Reactions in Battery Cathodes. *Adv. Energy Mater.* **2018**, *8* (20), No. 1800379.
- (91) Rong, Z.; Malik, R.; Canepa, P.; Gautam, G. S.; Liu, M.; Jain, A.; Persson, K.; Ceder, G. Materials Design Rules for Multivalent Ion Mobility in Intercalation Structures. *Chem. Mater.* **2015**, *27* (17), 6016–6021.
- (92) Xiong, P.; Kang, Y.; Yao, N.; Chen, X.; Mao, H.; Jang, W.-S.; Halat, D. M.; Fu, Z.-H.; Jung, M.-H.; Jeong, H. Y.; Kim, Y.-M.; Reimer, J. A.; Zhang, Q.; Park, H. S. Zn-Ion Transporting, In Situ Formed Robust Solid Electrolyte Interphase for Stable Zinc Metal Anodes over a Wide Temperature Range. *ACS Energy Lett.* **2023**, *8* (3), 1613–1625.
- (93) Li, S.; Huang, C.; Gao, L.; Shen, Q.; Li, P.; Qu, X.; Jiao, L.; Liu, Y. Unveiling the “Proton Lubricant” Chemistry in Aqueous Zinc-MoS₂ Batteries. *Angew. Chem., Int. Ed.* **2022**, *61* (50), No. e202211478.